

Egyptian Journal of Chemistry

http://ejchem.journals.ekb.eg/



Mechanosynthesis and Characterization of Nanostructured Mn-Al-B Permanent Magnets



Mohamed Khitouni*1, Adel Mishaal Al-Harbi,

Department of Chemistry, College of Science, Qassim University, Buraydah 51452, Saudi Arabia

Abstract

In this study, a high-energy ball-milling approach was used to process the mixture of α -Mn, Al, and B powders. Following the initial milling stage, the XRD patterns demonstrate that the Al and B atoms permeated the α -Mn matrix, resulting in the formation of an α -Mn(Al,B) solid solution as a consequence of the mechanical alloying process. With a percentage value of almost 85%, XRD showed that an amorphous phase had formed in favor of the Mn₂ AlB₂ -type phase when the milling period was increased to 30 h. There is a correlation between these XRD deductions and EDX elemental mapping. Additionally, it was found that the crystallite size decreased to roughly 10 nm and the lattice stresses increased to roughly 1.12% as the milling duration increased. The fine microstructure is associated with the defects' structure, which is characterized by a high dislocation density of around 20×10^{16} m⁻². The resulting nanometric microstructure, however, can be the result of substantial plastic deformation and the cumulative effects of solid solution. Understanding the microstructural behavior of Mn-Al-B alloys and how to optimize processing parameters to improve their microstructural features are two benefits of this research.

1. Introduction

The rising global demand for sustainable, cost-effective permanent magnets—prompted by electrification, renewable energy, and transportation—has heightened research into rare-earth-free magnetic materials. The availability, low cost, and promising inherent magnetic characteristics of manganese-aluminum (Mn-Al) alloys, and especially the metastable tetragonal τ -MnAl phase, make them interesting substitutes. However, the metastability of the τ phase, the challenge of creating phasepure and defect-controlled microstructures, and the relatively low coercivity in comparison to rare-earth magnets have all restricted the practical application of Mn-Al magnets in advanced energy conversion systems, modern electromechanical devices, and high-performance magnetic applications [1-3]. The potential and processing difficulties of Mn-Al systems are highlighted in recent reviews and experimental investigations, which encourage investigation of compositional modification and innovative synthesis methods to enhance performance [1,2]. To stabilize τ-MnAl and modify its microstructure and magnetic behavior, alloying additions have been used extensively. The ability of carbon additions (Mn-Al-C) to enhance coercivity and promote τ-phase formation, frequently through microstructure refinement and defect chemistry modification, makes carbon one of the most studied dopants. A less studied but potentially useful dopant is boron (B). According to multiple studies, trace amounts of B can affect magnetic hardening, phase formation, and grain refinement in related Mn-based systems. This suggests that Mn-Al-B alloys should be thoroughly studied as possible high-performance, rare-earth-free magnets. Furthermore, research on boron replacements and manganese borides in nearby Mn-based materials suggests that B can be important for bonding and magnetic coupling, which makes targeted Mn-Al-B studies logical [3-10]. In recent years, a number of non-equilibrium processing methods have been used to create Mn-Al alloys, such as mechanical milling (MM) [17– 19], drop synthesis [20], gas atomization [15], plasma arc discharge [16], splat quenching [13], magnetron sputtering [14], melt spinning [11,12], and splat quenching [17-19]. The most popular method among all of these is mechanical milling. This technique is used because it is comparatively easy and reasonably priced for making large amounts of Mn-Al powders [21]. High-energy ball milling, a well-known method with excellent scalability, has been studied to produce isotropic Mn-Al powders [22-26]. Grain boundaries and lattice defects are increased by pulverization, which improves coercivity [27]. The technique called "Mechanical Alloying (MA)" is the main purpose of the current research work. Ball milling produces close nanoscale mixing, high defect concentrations, and intense plastic deformation, which can accelerate the production of the t-MnAl phase and give management of grain size and phase distribution after the proper post-processing. Additional advantages of mechanosynthesis include its adaptability and compatibility with powder-based magnet building techniques [6-8]. The applicability of mechanosynthesis to Mn-Al-B development is supported by previous mechanical-milling investigations on

*Corresponding author e-mail: names@mail.com.; (Mohamed Khitouni).

Received Date: 18 October 2025, Revised Date: 07 November 2025, Accepted Date: 18 November 2025

DOI: 10.21608/EJCHEM.2025.433627.12486

©2026 National Information and Documentation Center (NIDOC)

Mn-Al and Mn-Al-C systems [4], which show significant increases in coercivity when processing and heattreatment parameters are optimized [5]. While carbon addition has long been used to stabilize the τ-MnAl phase and enhance coercivity in Mn-Al systems, recent studies have shown that boron doping offers distinct advantages. For example, recent work by Calvayrac et al. [4] reported improved magnetic properties in Mn-Al-C alloys, whereas Coey [5] specifically discussed the potential of Mn-Al-B alloys as rare-earth free permanent magnets and highlighted differences in microstructural refinement and phase evolution. Moreover, Prost [8] demonstrated that small boron additions lead to modified phase transformation kinetics compared with carbon. These findings indicate that boron may act differently than carbon not merely as a stabilizer of τ-phase but also as a grain-refinement and defect-engineering element—and therefore warrant focused investigation. The objective of this work is to synthesize and completely characterize mechanosynthesis-produced nanostructured Mn-Al-B powders and to clarify the connections between structure, processing, microstructure and defects characteristics. The particular motivations are as follows: (i) to assess if boron additions can help with τ -phase stabilization, and grain refinement in Mn-Al systems; (ii) to identify the best mechanosynthesis parameters that promote desired phase fractions and nanoscale microstructure; and (iii) to measure magnetic performance parameters (In a future work) in comparison to Mn-Al and Mn-Al-C equivalents documented in the literature [1]. To achieve these goals, we employ a systematic experimental plan: high-energy ball milling of Mn-Al-B powders under inert atmosphere; careful control of milling parameters to produce homogeneous nanostructured precursors. Structural characterization uses X-ray diffraction (XRD) with Rietveld refinement to determine phase content, lattice parameters, and lattice strain/crystallite size; scanning electron microscopy (SEM) for particle morphology; and EDS mapping to verify elements distribution and chemical state. These methods are selected to produce a comprehensive structure-processing-property dataset that isolates the role of B and mechanosynthesis conditions. The anticipated outcomes are (a) identification of milling conditions that maximize τ-phase formation in Mn-Al-B powders, (b) mechanistic insight into how B affects phase stability, grain size, and defects structure against referred Mn-Al and Mn-Al-C results.

2. Experimental

A. Raw materials and experimental process

Pure elemental powders of **manganese** (Mn, purity ~ 99.9%, particle size \leq 30 µm, supplied by Alpha Aesar), Aluminium (Al, purity ~99.9%, particle size \leq 40 µm, Alpha Aesar), and **Boron** (B, particle size \leq 20 µm, 99.7% purity)) were weighed separately and then mixed to obtain a composition (Mn₇₅Al₁₀B₅) (at%). The mechanical alloying process was carried out in a Fritsch planetary mill (Fritsch P7 model). Mechanical alloying was performed for up to 30 h under an argon atmosphere using hardened steel vials and balls, with a ball-to-powder mass ratio of 10:1 and a milling rotation speed of 600 rpm. The milling time 30 h was selected as the milling time limit because the phase evolution reached a quasi-steady state, with no further significant crystalline transformation detected beyond this stage. The Ar atmosphere was undertaken in a cycling process (first vacuum near 10^{-5} atm., second Ar addition to 1.1 atm.) performed three times. To prevent an excess in the internal vial temperature, the MA was performed in cycles (10 min on followed by 5 min off). Thus, a period of 30 h corresponds to 45 h of MA. After milling, the powders were extracted and handled inside an argon glove box to minimize any exposure to oxygen and avoid post-milling oxidation.

B. Characterization of material properties

X-ray diffraction (XRD) analyses were performed on a Siemens D-500 diffractometer (Berlin, Germany) using Cu K α radiation. The scans were recorded in a 2 θ angular range from 30° to 110°, with a fine angular step of 0.015°/second per position to measure the intensity of the Bragg peaks. The size of the crystallites as well as the network deformation were determined by Rietveld refinements using the MAUD software (version 2.8). Good refining is required to stabilize the microstructure and verify the functional behavior of these alloys. The quality of fitness is shown by the ratio of reliability parameters, or GoF (goodness of fit = R_{wp}/R_{exp}), where R_{wp} and R_{exp} stand for the weighted residual error and the expected error, respectively. The best refinements for this investigation were obtained when the GoF value was adjusted between 1.05 and 1.11. The morphology and chemical composition of the powders were studied using scanning electron microscopy (SEM) in secondary electron mode, with a DSM960A ZEISS model (Carl Zeiss GmbH, Oberkochen, Germany), operating at an acceleration voltage of 15 kV. The SEM system was equipped with an energy-dispersive spectroscopy (EDS) analyzer from Vega Tescan (Brno, Czech Republic). The particle size distribution was analyzed in detail using a particle analysis method in the ImageJ software (version 1.x) [28,29].

C. Theoretical

The Maud software, which includes several techniques for determining diffraction peak profiles, such as the Scherrer method, Williamson-Hall method, and Rietveld refinement, was used in the present investigation to evaluate the X-ray diffraction patterns [30]. A pseudo-Voigt (PV) function, which is a linear combination of a Gaussian (G) and a Lorentzian (L) function (Eq. 1), was used to fit each peak [31]:

$$PV(2\theta) = \gamma L(2\theta) + (1 - \gamma)G(2\theta)$$
 (Eq. 1)

where γ is an adjustable mixing parameter that describes the proportion of the Gaussian profile relative to the Lorentzian profile [32].

The Scherrer formula (Eq.2) [33,34] was used to determine the average crystallite size $\langle D \rangle$ after the Cu K α 2 radiation contribution was eliminated from the profiles:

$$\langle \mathbf{D} \rangle = \frac{k\lambda}{\beta_L \cos \theta}$$
 (Eq. 2)

where k is the shape factor, which varies depending on the crystal shape, λ is the wavelength of the CuK α 1 radiation, θ is the Bragg angle, and β_L is the Lorentzian component of the peak width, related to the reduced crystallite size.

The average microstrain (ε) was calculated using the tangential formula (Eq. 3) [33, 35]:

$$\langle \varepsilon \rangle = \frac{\beta_G}{4 \tan \theta}$$
 (Eq. 3)

where β_G is the Gaussian component of the peak broadening, resulting from microstrain present in the material.

The broadening of diffraction peaks as a function of the diffraction angle is used to calculate the average values of strain $\langle \epsilon \rangle$ and crystallite size $\langle D \rangle$ for the Rietveld method. The parameters D and ϵ are fitted using the formula in (Eq. 4) so that the theoretical model most closely resembles the experimental data:

$$\beta = \frac{k\lambda}{D\cos\theta} + 4\varepsilon \tan\theta$$
 (Eq. 4)

where β is the total peak broadening ($\beta = (\beta_L + \beta_G)$, in radians) at full width at half maximum (FWHM), K is the shape factor (or Scherrer constant, typically between 0.9 and 1), λ is the wavelength of the X-ray radiation, D is the average crystallite size, θ is the Bragg angle, and ε is the microstrain in the material.

Through a quantitative analysis method based on the integral intensity of the diffraction peaks, Maud software determines the relative proportion of each phase present in the sample using the intensities of the fitted peaks. The foundation of this technique is the idea that the amount of each phase is proportionate to the net area of the peaks in the diffraction pattern. The following formula (Eq. 5) is used to calculate the relative percentage of a given phase:

% **phase** =
$$\frac{I_{total}}{I_{phase}} \times 100$$
 (Eq. 5)

where I_{phase} is the integrated intensity of the peak corresponding to a specific phase, and I_{totql} is the sum of the integrated intensities of all peaks. The phases may be precisely quantified thanks to Maud software, which takes calibration in factors and experimental conditions into account. These findings are essential for interpreting crystallographic information and comprehending the sample's material characteristics.

3. Results and Discussion

A. Morphological Analysis during Mechanical Alloying

SEM and elemental mapping were used to analyze the microstructural changes of the Mn–Al–B powders during mechanical alloying, as illustrated in Fig. 1. A noticeable morphological change is seen in the SEM micrographs as the milling duration increases. Large, irregularly shaped particles that represent distinct elemental components are seen in the powder mixture at the first stage (0 h), with poor contact between them. Particle fragmentation and cold welding are seen after 2 and 4 h of milling, resulting in morphologies that are finer and more compact. Due to improved plastic deformation and interdiffusion between the Mn, Al, and B components, the powders show a notable decrease in particle size and an increase in homogeneity with additional milling up to 10–15 h. After 20 h of milling, the powders show a dense, homogeneous morphology with evenly spaced small particles, suggesting the development of a metastable solid solution. At 30 h milling, the morphology seems almost featureless, indicating full homogeneity and the achievement of a nanocrystalline structure.

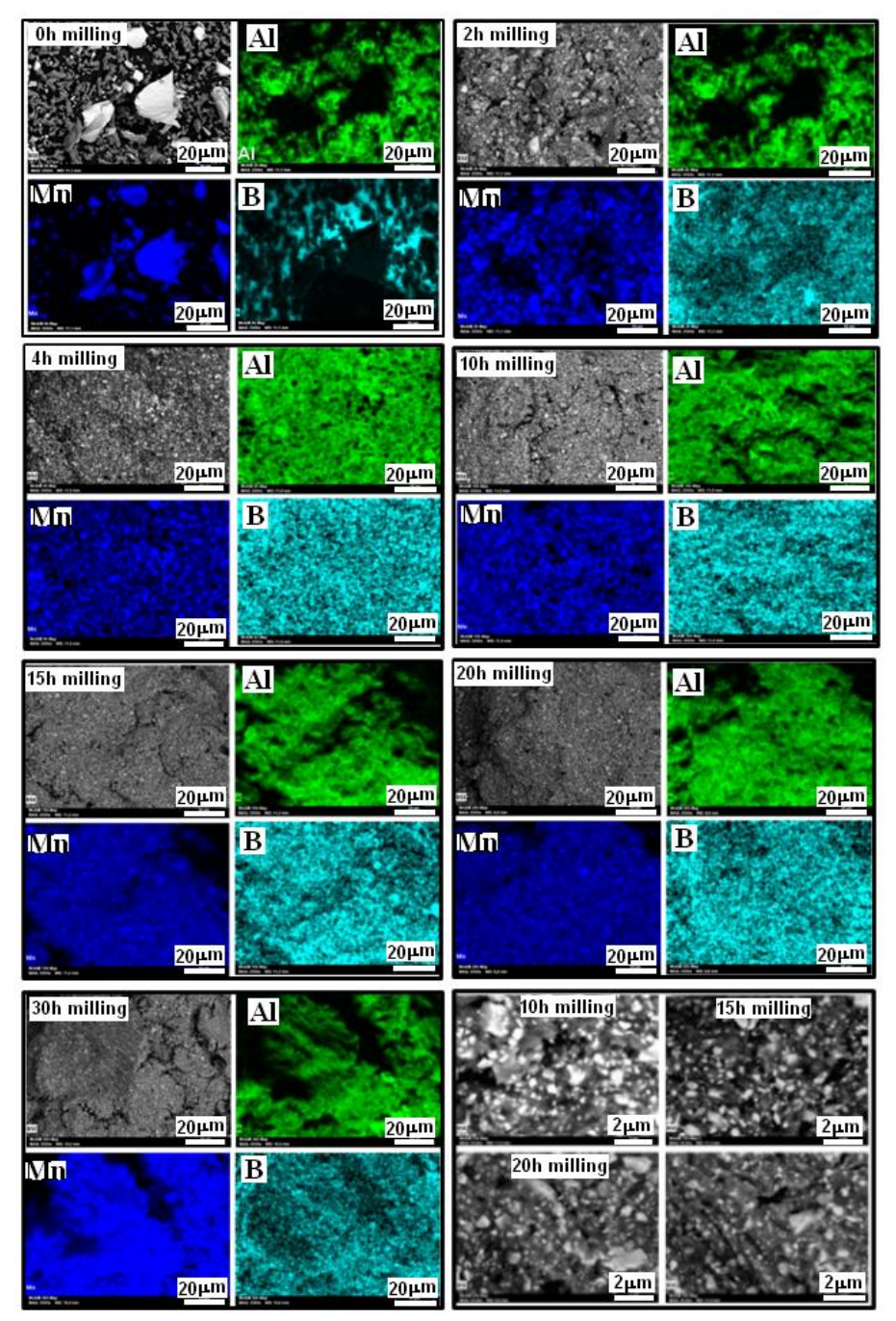


Figure 1. SEM images and elemental EDX mapping of the Mn-Al-B powders during selected milling times

These microstructural findings are further supported by the EDS elemental maps for Al, Mn, and B. The presence of different Mn and Al particles is reflected in the heterogeneous elemental distributions at 0h. The elemental difference becomes more consistent as the milling time increases to 4–10 h, indicating gradual alloying and mixing. Following 15 to 30 h, the maps display a consistent distribution of Al, Mn, and B throughout the analyzed areas, signifying effective solid-state diffusion and the creation of a chemically homogeneous alloy. In accordance with the usual behavior of mechanically alloyed systems, this evolution demonstrates that extended milling enhances atomic intermixing and alloy formation through repeated fracturing and cold welding cycles [36–38]. It should be noted that boron EDS contrast is enhanced only for visualization purposes, because boron quantification by EDS is limited due to its low characteristic X–ray energy.

High-resolution SEM images of the Mn–Al–B powders milled for 10, 15, 20, and 30 h (see bottom right of Figure 1) reveal the progressive morphological evolution during mechanical alloying. The powder particles assume an irregular and coarse shape with heterogeneous contrast, indicating incomplete alloying and limited interdiffusion between elements. After

15 h of milling, one can see finer and more equiaxed particles with better homogeneity, attributed to intensified cold welding and fracturing processes. At 20 h, the powders exhibit a compact and uniform morphology, suggesting an advanced stage of alloy formation. After 30 h, the microstructure becomes almost homogeneous, with nanosized and well-dispersed particles, confirming the development of a single-phase Mn–Al–B solid solution. This progressive refinement and homogenization with extended grinding time aligns well with the typical behavior of mechanically alloyed systems, where repeated deformation and interdiffusion drive solid-state reactions.

B. XRD analysis

Figure 2 displays X-ray diffraction patterns of the Mn–Al–B powder mixtures as a function of milling time. Figure 3 also displays the Rietveld refinements of the obtained XRD patterns after different milling times. The crystalline character of the initial powders is demonstrated by the distinct and intense peaks in the diffractogram at 0 h of milling, which correspond to the elemental α -Mn (Space group: $I\bar{4}3m$, a=8.9125(1) Å [36]) and Al (Space group: $Fm\bar{3}m$, a=4.0504(4) Å [37]) and B (space group: $R\bar{3}m$, a=5.5940(1) Å and c=12.0756(1) Å [38]) phases. The diffraction peaks expand and decrease in intensity after 2h of milling, indicating the beginning of lattice strain and structural refinement brought on by repeated cold welding and fracturing. Grain size reduction and increased defect density are confirmed by the diffraction peaks becoming increasingly broader and less intense as the milling time increases from 10 to 15 h. The peaks of the initial components almost vanish after 20 h of milling, and broad humps arise, indicating the development of an amorphous-like phase or metastable solid solution. A single broad feature appears in the XRD pattern after 30 h, suggesting significant alloying and the potential development of a nanocrystalline Mn–Al-based phase with uniform boron inclusion. In accordance with previously reported behavior in comparable mechanically alloyed systems [39–41], this structural evolution shows that extended mechanical alloying efficiently promotes diffusion and solid-state reactivity between Mn, Al, and B.

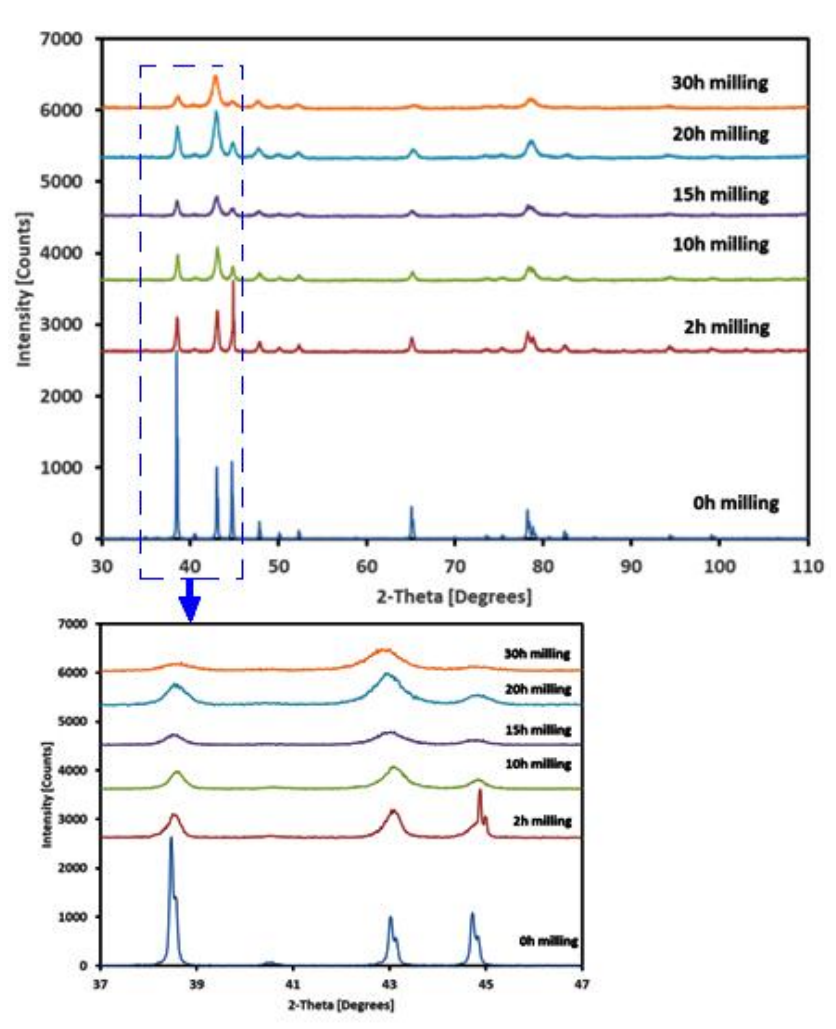


Figure 2. XRD patterns of the Mn-Al-B powders during selected milling times

The phase evolution deduced from the basic patterns is quantitatively supported by the Rietveld refinement of the XRD data. The Rietveld refinements of the XRD patterns for Mn-Al-B mixture powders as a function of milling times are shown in Figure 3. The goodness-of-fit (GOF) refinement parameter is approximately 1.11, which validates the accuracy of the suggested structural models and phase fractions. The diffraction profiles for 2h of milling can be mostly attributed to the α-Mn (Space group: $I\overline{4}3m$, a=8.9291(1)Å) phase, suggesting that manganese is still the main crystalline component and that the alloying process is continuing. As the milling time increases to 10 h, the α -Mn reflections get weaker and new diffraction peaks that correspond to the α - Mn(Al) (space group: $I\overline{4}3m$, a=8.9543(1) Å) and the MnB₂ [42] (space group: P6/mmm, a=3.0050(1) and c=3.0380(1) Å and wt%=28.07) intermetallic phases eventually emerge. The improved solid-state diffusion and reaction kinetics facilitated by multiple cold-welding and fracture events during mechanical alloying are reflected in this change. The structure partially amorphized and a nanocrystalline Mn₂ AlB₂ -type phase [43] (Space group: Cmmm, a=2.9201(1), b=11.0810(1) and c=2.8911 (1) Å and wt%=54.96) forms with an amorphous matrix after 20h of milling, as seen by the diffraction peaks broadening considerably and the appearance of a diffuse background. The validity of the structural models used is confirmed by the good agreement between the predicted and experimental profiles, which is shown by matching peak positions and low residuals (Fig. 3). These results demonstrate that mechanical alloying efficiently accelerates the phase change from α-Mn to the Mn₂ AlB₂ at 20 h of milling through an intermediate MnAl-rich stage, comparable with recent research on Mn-Al-B systems subjected to extended high-energy milling [11,40]. Together, these quantitative results quantify the simultaneous grain refinement and strain accumulation that explain the observed amorphization and peak broadening in the XRD patterns. Lattice parameters for the nanocrystalline Mn₂ AlB₂ -type phase that result from prolonged milling durations are a=2.9490(1), b=11.0824(1), and c=2.8591(1) Å and a=2.9670(1), b=11.0920(1), and c=2.8742 (1) Å for 20 and 30 h, respectively. By increasing the milling time up to 30 h, the proportion of the amorphous phase increases in favor of the Mn₂ AlB₂ -type phase, and its proportion reaches a value of about 85% (Fig. 4).

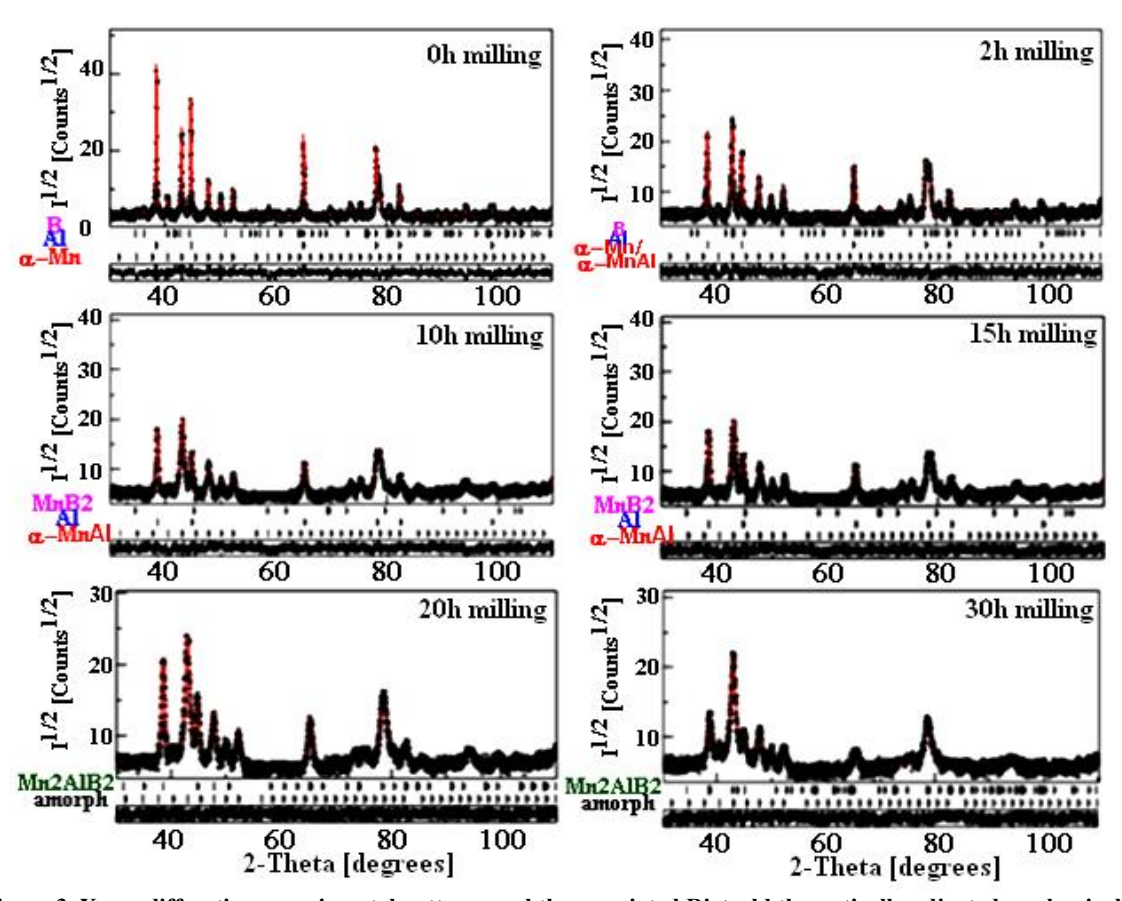


Figure 3. X-ray diffraction experimental patterns and the associated Rietveld theoretically adjusted mechanically alloyed MnAlB powders collected after selected milling times

The phase proportion evolution of the Mn-Al-B mixture powders as a function of milling time is calculated by refining XRD diffraction patterns with the MAUD software. The results are shown in Figure 4. The powder mixture at 0 h of milling is composed of α -Mn, Al, and B in proportions of 50, 35, and 15%, respectively. Their proportions gradually decrease to roughly 47, 32, and 11%, respectively, after 2h of milling, indicating the beginning of solid-state processes and the progressive diffusion of the initial components. The onset of solid solution formation is indicated by the detection of a small proportion of α -Mn(Al,B) (~10%) at this stage. It should be noted that the α -MnAl phase refined here corresponds to a solid solution of Al in the α-Mn lattice; boron incorporation at this milling stage cannot be confirmed by XRD due to the very low scattering factor of B, and therefore no distinct α-Mn(Al,B) diffraction peaks are expected. When the milling time is increased to 10 h, the diffraction data shows the appearance of broad intensity that can be reasonably modeled in the Rietveld refinement using a MnB₂ -type boride component (~28%). However, due to the absence of the characteristic sharp reflections expected for wellcrystallized MnB₂ (20 ~ 35°, 41°, and 62°), this contribution should be regarded as indicative of a poorlycrystalline/nanocrystalline boron-rich environment rather than a fully resolved crystalline MnB2 phase. This boron-rich contribution coexists with Mn and Al as well as the α-Mn(Al) solid solution. At 15 h of milling, the modeled MnB₂ -type fraction increases to ~45%, while the α -Mn(Al) phase rises to ~55%. After 20 h, the initial α -Mn, Al and B phases are almost entirely consumed, and a Mn₂ AlB₂ -type intermetallic contribution becomes dominant (~35%) together with a large amorphous fraction (~65%). The amorphous fraction obtained from Rietveld is therefore considered semi-quantitative, since amorphous components are introduced as broad background contributions rather than indexed phases, and transient peak sharpening stages may reflect short-range relaxation rather than recrystallization of well-defined crystalline phases. For further milling times up to 30 h, the Mn₂ AlB₂ fraction decreases to ~15%, while the amorphous component increases significantly to ~85%. This evolution reflects extensive amorphization and structural disorder generated by repeated fracture, cold welding and re-welding events during high-energy milling. Thus, the mechanosynthesis of the Mn-Al-B mixture proceeds from the initial crystalline elemental mixture (Mn, Al, B) through transient solid solution and boron-rich poorly-crystalline intermediate states (modeled as MnB₂ -type) and the Mn₂ AlB₂ -type contributions, before evolving ultimately toward a predominantly amorphous structure after 30 h. The phase fraction at 30 h therefore represents a predominantly amorphous/nanocrystalline state rather than a fully amorphous material, and its fraction extracted from Rietveld should be considered semi-quantitative. The large amorphous fraction (~85%) is advantageous as it serves as a metastable, highly reactive precursor that can crystallize efficiently toward the desired τ-MnAl phase during thermal treatment steps used in magnet fabrication.

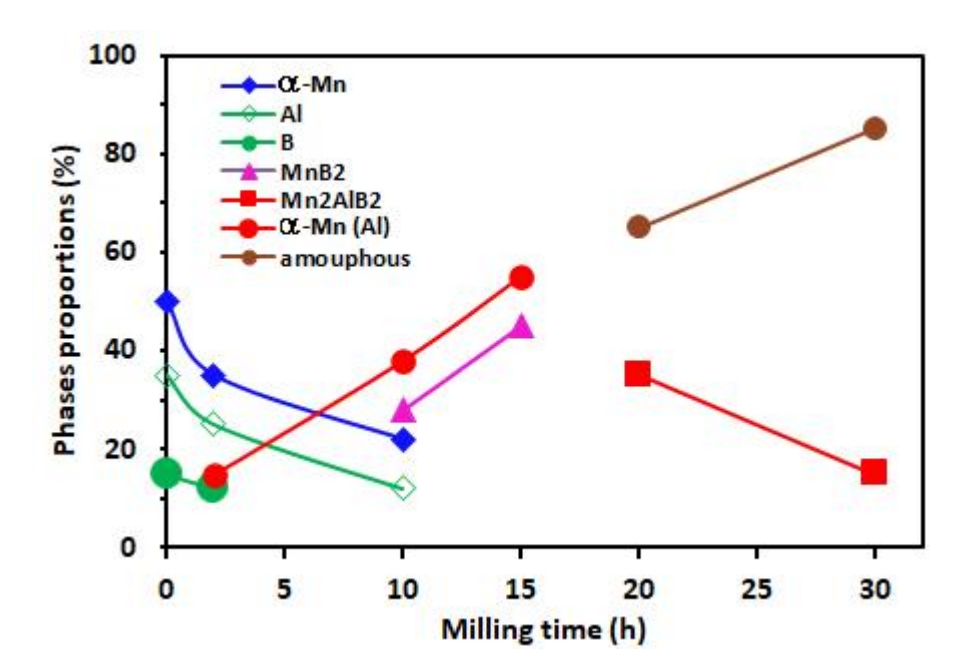


Figure 4. Variation of the refined phases proportions of the MnAlB mixture powders as a function of milling time

The changes in crystallite size and lattice strains for the different phases in the Mn–Al–B powder mixture as a function of milling duration are shown in Figs. 5 and 6. All phases exhibit a significant decrease in crystallite size during the initial h of mechanical alloying, reaching less than 50 nm during 10 h of milling accompanied by a marked increase in lattice strain up to 0.6%. The severe plastic deformation and continual fracturing–welding events occurring during high-energy milling conditions are responsible for the rapid refining. The formation of a nanocrystalline structure is shown by the stabilization of the crystallite sizes of α -Mn and the newly generated MnB₂ phase around 20–25 nm after further milling up to 15 h, while lattice strains reaching about 0.8–0.9 %, confirming that the system experiences substantial internal stresses and

structural disorder. After 20 h of milling, the Mn₂ AlB₂ intermetallic phase forms as a result of the gradual diffusion between the Mn, Al, and B atoms. Its initial crystallite size is close to 25 nm. The crystallite size of this phase is further reduced to about 10 nm after milling for up to 30 h. Its lattice strain increases to approximately 1.12 %. The elevated strain levels in the Mn₂ AlB₂ suggest that the phase forms under highly non-equilibrium conditions, characterized by severe lattice deformation and enhanced atomic mobility. Such microstructural refinement and lattice strain accumulation provide a strong driving force for solid-state diffusion and phase transformation, facilitating the synthesis of nanocrystalline Mn₂ AlB₂ directly through mechanical alloying. On the other hand, the resulting microstructural features, including nanometric grain size and high defect density, are known to enhance reactivity and diffusion kinetics, thus accelerating solid-state reactions between Mn, Al, and B atoms. For instance, it has been shown that melt-spun and mechanically-processed Mn-Al-C materials produce nanocrystalline microstructures and undergo pronounced phase evolution during subsequent heat treatments [11,44]. In Mn-Al-C and Mn-Al systems, severe plastic deformation during ball milling or rapid solidification results in very fast crystallite size reduction and promotes the formation of metastable or nanocrystalline magnetic phases. Similar mechanistic characteristics have been identified for the Fe-Mn and the Fe-Mn-Al alloys produced via mechanical alloying; prolonged milling results in the formation of finely dispersed secondary phases or the dissolution of elemental constituents into solid solutions, with grain sizes reaching the nanoscale and XRD peak broadening indicating severe lattice distortion and reduced coherent domain size. The relationship between milling time, microstructural refinement, and the kinetics of subsequent solidstate processes is supported by these investigations [45].

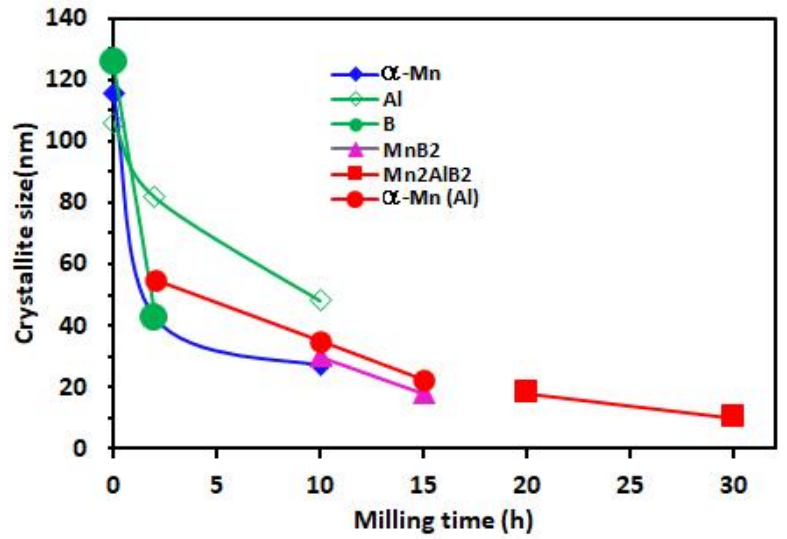


Figure 5. Variation of crystallite sizes of MnAlB mixture powders as a function of milling time

According to several studies, pre-milling Mn-Al-B precursor powders improve reactivity and increases phase-conversion efficiency in further synthesis approaches, specifically for the Mn_2 AlB₂ type phase. In SHS methods, longer milling times were observed to increase phase purity and lower the necessary peak temperatures. This suggests that the solid-state formation of Mn_2 AlB₂ is accelerated by the progressive refinement of crystallites and the increased interfacial area created by milling. The idea that Mn_2 AlB₂ emerges with prolonged milling (20 h) and refines further with additional milling to reach sub-20 nm crystallite sizes is supported by these observations [46, 47]. The final observation is that (i) compositional homogenization at the nanoscale and (ii) a significant increase in defect density (dislocations, grain boundaries, etc.) accelerate diffusion and reaction kinetics in mechanically activated systems, according to mechanistic studies that measure element dissolution and grain refinement during high-energy ball milling. This offers a microstructural explanation for the simultaneous decrease in crystallite size and the gradual emergence of the Mn_2 AlB₂ intermetallic. Moreover, the substantial lattice strain accumulated during milling is a key factor that enhances reactivity and diffusion, ultimately enabling the formation of a fine-grained Mn_2 AlB₂ -type structure.

Fecht [48] claimed that the generation and the movement of dislocations could decrease grain size. Rawers and Cook [49] showed that the strain on the nanograin boundary could extend into nanograin, expanding the lattice. So, for MA samples subjected to severe plastic deformation, dislocations are the main defects, and this dislocation density, ρ , can be represented in terms of D and ϵ by the Eq. 5 [50–52]:

$$\rho_d = \frac{2\sqrt{3}\,\varepsilon}{Db} \tag{Eq. 5}$$

where ε is the lattice strain, D is the crystallite size, and b is the Burgers vector magnitude corresponding to the $[\frac{1}{2}\langle 110\rangle]$ dislocation type ($b = \frac{a}{\sqrt{2}}$). The above formula gives a good average estimation for the present polycrystalline tetragonal

 Mn_2 AlB₂ phase, even though it is derived for isotropic cubic systems. The dislocation density (ρ_d) in the powders of the Mn-Al-B mixture changes with milling time, as shown in Figure 7. After the first 15 h, the dislocation density (ρ_d) rises linearly from roughly $0.05 \times 10^{16} / m^2$ to $15 \times 10^{16} / m^2$, followed by a little increase of $20 \times 10^{16} / m^2$ between 20 and 30 h of milling. In the crystal system close to grain boundaries, dislocations were typically the primary cause of microstructure refinement. The composition of the powder mixture appears to have an impact on the dislocation density in addition to the severe plastic deformation effect caused by the high-energy mechanical alloying. In fact, significant plastic deformation and the cumulative effects of solid solution $(\frac{R_{All}}{R_{Mn}} = 1.125)$ may be the cause of the linear increase in dislocation.

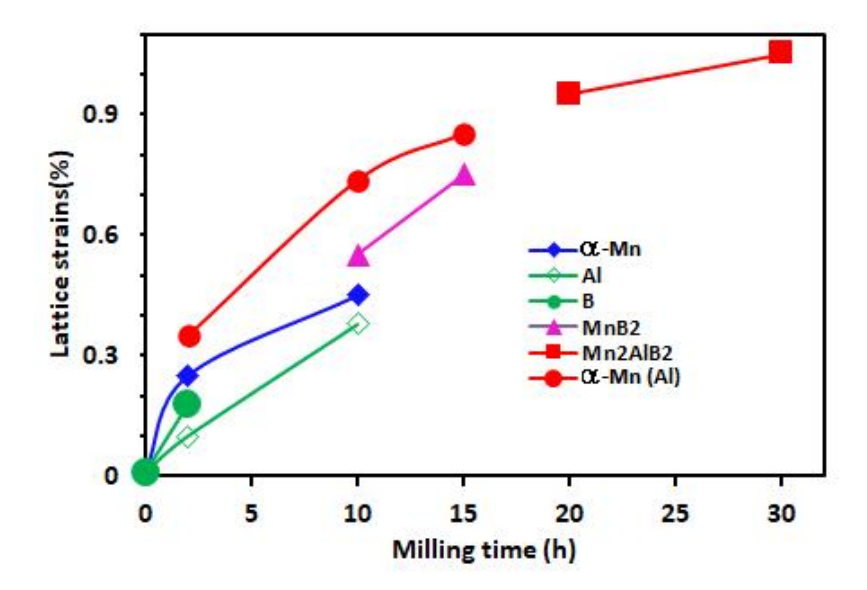


Figure 6. Variation of lattice strain levels of the MnAIB mixture powders as a function of milling time

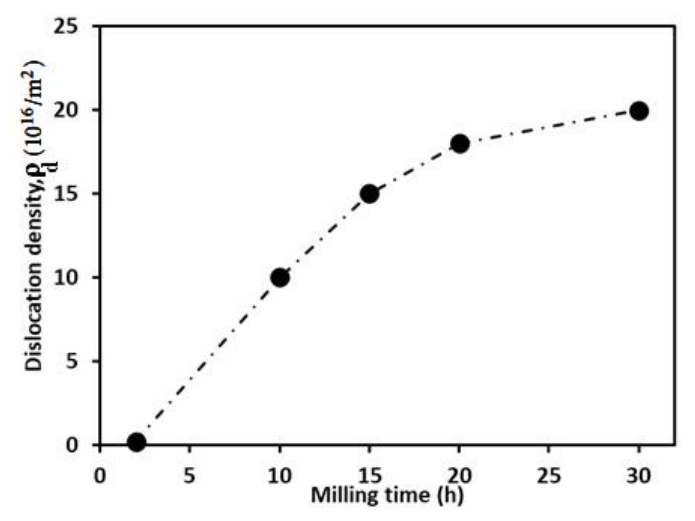


Figure 7. Variation of dislocation density of MnAlB mixture powders as a function of milling time

4. Conclusions

In the present study, the mixture of the α -Mn, Al and B powders was processed by a high-energy ball-milling technique. After early stage of milling, it is clear from the XRD patterns that Al and B atoms diffused throughout the α -Mn matrix, forming an α -Mn(Al,B) solid solution as a result of the mechanical alloying process. Upon increasing milling time to 30 h, XRD revealed the formation of an amorphous phase in favor of the Mn₂ AlB₂ -type phase with a proportion value of about 85%. These XRD deductions are correlated with EDX elemental mapping. Furthermore, it was discovered that the increase in milling time led to a decrease in the crystallite size to about 10 nm and an increase of lattice strains to about 1.12%.

The fine microstructure is associated to the structure of defects which characterized by a high dislocation density with value about 20×10^{16} m⁻². However, significant plastic deformation and cumulative effects of solid solution may be the cause of the obtained nanometric microstructure. These findings contribute to understanding the microstructural behavior of the Mn-Al-B alloys and provide insights into optimizing processing parameters to enhance their microstructural properties.

5. Conflicts of interest

There are no conflicts to declare.

6. Formatting of funding sources

Not applicable.

7. Acknowledgments

The authors gratefully acknowledge Qassim University, represented by the Deanship of Graduate Studies and Scientific Research, on the financial support of this research under the number QU-J-PG-2—2025-53867, during the academic year 1446 AH / 2024 AD.

8. References and Bibliography

- [1] Kontos, S.; Goll, D.; Gutfleisch, O. An overview of Mn–Al permanent magnets with a study on their structure and magnetic properties. Energies 2020, 13 (21), 5549.
- [2] Crisan, A. D.; Isnard, O.; Popa, S. Magnetism and ε - τ phase transformation in MnAl-based alloys. Mater. 2021, 14, 3231.
- [3] Song, S.; He, Y. Rare earth free Mn-Al and Mn-Bi magnetic materials: A review, Journal of Magnetism and Magnetic Materials, 2025, 628, 173187.
- [4] Calvayrac, F.; Martínez, L.; Dupuis, A. Mechanical alloying and theoretical studies of Mn–Al(C) magnets. Intermetallics 2018, 98, 15–22.
- [5] Coey, J.M.D. Rare-earth-free permanent magnets: The case of Mn-Al-C, AIP Advances, 2022, 12, 115101
- [6] Zhang, X.; Li, Q.; Sun, Y. Driving rapid atomic order in MnAl via low-magnitude magnetic field annealing. Acta Mater. 2025, 266, 119292.
- [7] Ibn Gharsallah, HA; zabou, M.; Escoda, L; Suñol, J.J.; López, I.; Llorca-Isern, N; Khitouni, M. The magnetic and structural properties of nanostructured (Fe75Al25) 100-xBx alloys prepared by mechanical alloying. Journal of Alloys and Compounds. 2017, 729, 776-786.
- [8] Prost, T. Magnetic properties study of the Mn–Al system with additions of B or C and mechanical milling techniques. Technical Report, Ames Laboratory, U.S. Department of Energy, 2012.
- [9] Gutfleisch, O.; Willard, M. A.; Brück, E.; Chen, C. H.; Sankar, S. G.; Liu, J. P. Magnetic materials and devices for the 21st century: Stronger, lighter, and more energy efficient. Adv. Mater. 2011, 23, 821–842.
- [10] Li, W.; Zhang, P. Effect of boron doping on the magnetic and structural properties of Mn–Al-based alloys. J. Alloys Compd. 2023, 939, 168888.
- [11] Fazakas, E.; Varga, L. K.; Mazaleyrat, F. Preparation of nanocrystalline Mn–Al–C magnets by melt spinning and subsequent heat treatments. J. Alloys Compd. 2007, 434, 611–613.
- [12] Liu, Z. W.; Chen, C.; Zheng, Z. G.; Tan, B. H.; Ramanujan, R. V. Phase transitions and hard magnetic properties for rapidly solidified Mn–Al alloys doped with C, B, and rare earth elements. J. Mater. Sci. 2012, 47, 2333–2338.
- [13] Kim, Y. J.; Perepezko, J. H. Formation of a metastable ferromagnetic τ phase during containerless melt processing and rapid quenching in Mn–Al–C alloys. J. Appl. Phys. 1992, 71 (2), 676–680.
- [14] Duan, C. Y.; Qiu, X. P.; Ma, B.; Zhang, Z. Z.; Jin, Q. Y. The structural and magnetic properties of τ- MnAl films prepared by Mn/Al multilayers deposition plus annealing. Mater. Sci. Eng. B 2009, 162 (3), 185–188.
- [15] Lee, J. G.; Wang, X. L.; Zhang, Z. D.; Choi, C. J. Effect of mechanical milling and heat treatment on the structure and magnetic properties of gas atomized Mn–Al alloy powders. Thin Solid Films 2011, 519 (23), 8312–8316.
- [16] Lee, J. G.; Li, P.; Choi, C. J.; Dong, X. L. Synthesis of Mn–Al alloy nanoparticles by plasma arc discharge. Thin Solid Films 2010, 519 (1), 81–85.
- [17] Chaturvedi, A.; Yaqub, R.; Baker, I. A comparison of τ- MnAl particulates produced via different routes. J. Phys.: Condens. Matter 2014, 26 (6), 064201.
- [18] Obi, O.; Burns, L.; Chen, Y.; Fitchorov, T.; Kim, S.; Hsu, K.; Heiman, D.; Lewis, L. H.; Harris, V. G. Magnetic and structural properties of heat-treated high-moment mechanically alloyed Mn–Al–C powders. J. Alloys Compd. 2014, 582, 598–602.

- [19] Obi, O.; Burns, L.; Chen, Y.; Bennett, S.; Sawicki, M.; Kaplan, D.; Arango, A. M.; Lewis, L. H.; Harris, V. G. Effect of ambient aging on heat-treated mechanically alloyed Mn–Al–C powders. IEEE Trans. Magn. 2013, 49 (7), 3372–3374.
- [20] Fang, H.; Cedervall, J.; Hedlund, D.; Shafeie, S.; Deledda, S.; Olsson, F.; von Fieandt, L.; Bednarcik, J.; Svedlindh, P.; Gunnarsson, K.; Sahlberg, M. Structural, microstructural and magnetic evolution in cryomilled carbon-doped MnAl. Sci. Rep. 2018, 8 (1), 2525.
- [21] Saravanan, P.; Vinod, V. T. P.; Černík, M.; Selvapriya, A.; Chakravarty, D.; Kamat, S. V. Processing of Mn–Al nanostructured magnets by spark plasma sintering and subsequent rapid thermal annealing. J. Magn. Magn. Mater. 2015, 374, 427–432.
- [22] Cui, J.; Kramer, M.; Zhou, L.; Liu, F.; Gabay, A.; Hadjipanayis, G.; Balasubramanian, B.; Sellmyer, D. Current progress and future challenges in rare- earth- free permanent magnets. Acta Mater. 2018, 158, 118–137.
- [23] Bittner, F.; Schultz, L.; Woodcock, T. G. The role of interface distribution in the decomposition of metastable L1 $_{\circ}$ Mn $_{\circ}$ 4 Al4 $_{\circ}$. J. Alloys Compd. 2017, 727, 1095–1099.
- [24] Rial, J.; Palmero, E. M.; Bollero, A. Efficient nanostructuring of isotropic gas- atomized MnAl powder by rapid milling (30 s). Eng. 2020, 6 (2), 173–177.
- [25] Attyabi, S. N.; Radmanesh, S. M. A.; SeyyedEbrahimi, S. A.; Dehghan, H.; Lalegani, Z.; Hamawandi, B. Stress- induced grain refinement in hard magnetic Mn_{5 2} Al_{4 5 .7} C_{2 .3} fabricated using the ball- milling method. Mater. 2022, 15 (22), 7919.
- [26] Jo, J.; Vishwanadh, B.; Shankar, M. R.; Wiezorek, J. M. K. Microstructure and magnetic properties of binary Mn₅ 4 Al_{4 6} alloy particulates obtained by severe plastic deformation processing via end-milling and annealing. J. Magn. Magn. Mater. 2023, 586, 171200.
- [27] Yang, J.; Yang, W.; Shao, Z.; Liang, D.; Zhao, H.; Xia, Y.; Yang, Y. Mn-based permanent magnets. Chinese Phys. B 2018, 27 (11), 117503.
- [28] Bakas, G.; Dimitriadis, S.; Deligiannis, S.; Gargalis, L.; Skaltsas, I.; Bei, K.; Karaxi, E.; Koumoulos, E. P. A tool for rapid analysis using image processing and artificial intelligence: Automated interoperable characterization data of metal powder for additive manufacturing with SEM case. Metals 2022, 12, 1816.
- [29] Khitouni, M.; Kolsi, A. W.; Njah, N. Crystallite refinement of NiAl powders during mechanical milling. Ann. Chim. Sci. Mat. 2003, 28, 17–29.
- [30] Le Caer, G.; Delcroix, P.; Begin-Colin, S.; Ziller, T. High-energy ball-milling of alloys and compounds. Hyperfine Interact. 2002, 141, 63–72.
- [31] Degen, T.; Sadki, M.; Bron, E.; König, U.; Nenert, G. The HighScore suite. Powder Diffr. 2014, 29, S13-S18.
- [32] Qin, X. Y.; Zhang, W.; Zhang, L. D.; Jiang, L. D.; Liu, X. J.; Jin, D. Low-temperature resistance and its temperature dependence in nanostructured silver. Phys. Rev. B 1997, 56, 10596.
- [33] Sekri, A.; Mhadhbi, M.; Escoda, L.; Sunol, J. J.; Khitouni, M.; Makhlouf, T. Synthesis and structural characterization of nanocrystalline Fe- Ni- Zr- B alloy prepared by powder metallurgy. J. Tunis. Chem. Soc. 2015, 17, 49–56.
- [34] Kaloshkin, S. D.; Tcherdyntsev, V. V.; Tomilin, I. A.; Baldokhin, Y. V.; Shelekhov, E. V. Phase transformations in Fe–Ni system at mechanical alloying and consequent annealing of elemental powder mixtures. Physica B 2001, 299, 236–241.
- [35] Hong, L. B.; Fultz, B. Two-phase coexistence in Fe-Ni alloys synthesized by ball milling. J. Appl. Phys. 1996, 79, 3946–3955.
- [36] Gazzara, C. P.; Middleton, R. M.; Weiss, R. J.; Hall, E. O. A refinement of the parameters of alpha manganese locality: synthetic sample at T = 298 K. Acta Crystallogr. A 1967, 22, 859–862.
- [37] Woodward, P. M.; Karen, P. Mixed valence in YBaFe₂ O₅ . Inorg. Chem. 2003, 42, 1121–1129.
- [38] Parakhonskiy, G.; Dubrovinskaia, N.; Bykova, E.; Wirth, R.; Dubrovinsky, L. High pressure synthesis and investigation of single crystals of metastable boron phases: Note: epsilon-trigonal phase. High Press. Res. 2013, 33, 673–683.
- [39] Benjamin, J. S. Metallurgical Trans. Metall. Trans. 1970, 1, 2943–2951.
- [40] Suryanarayana, C. Progress in Materials Science. Prog. Mater. Sci. 2001, 46, 1–184.
- [41] Zhang, J.; Li, X.; Liu, Y.; Wang, J. Microstructural evolution and phase formation during mechanical alloying of Mn–Al- based systems. J. Alloys Compd. 2017, 725, 628–636.
- [42] Bown, A. L.; Nereson, N. G. Manganese boride, MnB₂ . AIP Conf. Proc. 1974, 34, 34–36.

- [43] Becher, H. J.; Peisker, E.; Krogmann, K. Über das ternäre Borid Mn₂ AlB₂ . Z. Anorg. Allg. Chem. 1966, 344, 140–147.
- [44] Zeng, Q.; Baker, I.; Cui, J. B.; Yan, Z. C. Structural and magnetic properties of nanostructured Mn–Al–C magnetic materials. J. Magn. Magn. Mater. 2007, 308, 214–226.
- [45] Liu, T.; Liu, H. Y.; Zhao, Z. T.; Ma, R. Z.; Hu, T. D.; Xie, Y. N. Mechanical alloying of Fe–Mn and Fe–Mn–Si. Mater. Sci. Eng. A 1999, 271 (1–2), 8–13.
- [46] Merz, J.; Richardson, P.; Cuskelly, D. Formation of Mn₂ AlB₂ by induction- assisted self- propagating high- temperature synthesis. Open Ceram. 2021, 8 (7), 100190.
- [47] Yakovtseva, O. A.; Emelina, N. B.; Mochugovskiy, A. G.; Bazlov, A. I.; Prosviryakov, A. S.; Mikhaylovskaya, A. V. Effect of mechanical alloying on the dissolution of the elemental Mn and Al–Mn compound in aluminum. Metals 2023, 13 (10), 1765.
- [48] Fecht, H.- J. Nanostructure formation by mechanical attrition. Nanostructured Mater. 1995, 6 (1-4), 33-42.
- [49] Rawers, J.; Cook, D. Influence of attrition milling on nanograin boundaries. Nanostructured Mater. 1999, 11 (3), 331–342.
- [50] Williamson, G. K.; Smallman, R. E. Dislocation densities in some annealed and cold- worked metals from measurements on the X- ray Debye Scherrer spectrum. Philos. Mag. 1956, 1 (1), 34–46.
- [51] Bachaga, T.; Daly, R.; Escoda, L.; Sunol, J.J.; Khitouni. M. Amorphization of Al₅₀(Fe₂B)₃₀Nb₂₀ Mixture by Mechanical Alloying, Metallurgical and Materials Transactions A, 2013, 44A, 4718-4724
- [52] Zhao, Y. H.; Shang, H. W.; Lu, K. Microstructure evolution and thermal properties in nanocrystalline Fe during mechanical attrition. Acta Mater. 2001, 49, 365–375.